Advances in Surface Modification via Laser Crystallization

Y. Lawrence YAO, Andrew J. BIRNBAUM, Anubha BHATLA and Gen SATOH

Department of Mechanical Engineering, Columbia University, 220 Mudd Bldg. MC 4703, New York, NY 10027, USA
E-mail: yly1@columbia.edu

This presentation reviews recent work in laser manipulation of crystallinity of NiTi shape memory alloy thin films as well as biodegradable polymers. Amorphous sputter-deposited NiTi films are processed using pulsed, melt-mediated laser crystallization techniques to control the spatial distribution of crystalline zones. Since shape memory responses stem from crystallographic shifts, only the selectively crystallized regions exhibit these properties. This process provides not only spatial control over the shape memory response, but potentially, through proper use of operational parameters, the shape memory response itself, i.e. phase transformation temperature, transformation strain, recovery stress etc. The effects of processing parameters on the shape memory and mechanical response are discussed.

Crystallinity of semi-crystalline polymers such as aliphatic homopolymer poly (L-lactic acid) (PLLA) affects their degradation and physical properties. The effects of laser irradiation on the crystallinity, long-range order and short-range conformations at the surface of PLLA films are investigated. Detailed characterization of the effect of laser treatment is accomplished using microscopy, X-ray diffraction and Infrared spectroscopy. Rapid melting at the surface, quench rates in the process, multiple thermal cycles, superheating and heat accumulation due to pulsed nature of the process and primarily regime II kinetics of PLLA contribute to an overall reduction in crystallinity.

Keywords: Laser crystallization, shape memory, polymer degradation, thin film

1. Introduction

With so many attributes and properties of materials being defined by their microstructures, control over the crystallinity of materials is vital to enhancing the performance of advanced materials. Two applications of lasers to the modification of surface crystallinity are discussed below. One application uses excimer laser pulses to crystallize amorphous NiTi thin films to selectively impart shape memory properties. The second application utilizes a pulsed Nd:YAG laser to reduce the crystallinity of polymer films to control degradation rates.

2. Excimer Laser Crystallization of Amorphous NiTi

Although shape memory alloys' (SMA's) non-conventional properties have been studied extensively over the last four decades, their actual implementation has been limited due to several complicating factors. A main impediment to application, particularly for thermally induced macro-scale actuation applications is poor dynamic response stemming from long heat dissipation times. Recently, thin film shape memory structures have received increasing attention for micro-scale actuation as they do not suffer from this limitation due to their exceedingly low thermal mass. In addition to the shape memory effect, significant attention has also been devoted to exploiting the superelastic effect. In particular, applications in improving the wear resistance of NiTi surfaces have received increasing amounts of interest [1-3].

Several investigations on the use of laser annealing in order to control the spatial extents of crystalline regions have been conducted, although they have all been restricted to CW, solid phase processing. Bellouard et. al. [4,5] used a near IR CW laser to selectively solid-phase crystallize a sputter deposited NiTi thin film for the purposes of fabricating a micro-gripper whose only active component was the crystallized portion of the device. He et. al. [6] investigated the use of a CW CO_2 laser to selectively anneal a NiTi thin film via solid-phase crystallization as well.

This work proposes the use of pulsed, melt-mediated laser crystallization techniques to control the spatial distribution of crystalline zones within an amorphous or pre-crystallized matrix. This process can provide not only spatial control over the shape memory response, but through proper use of operational parameters, has the potential for tailoring the shape memory response itself, i.e. phase transformation temperature, transformation strain, recovery stress etc. The use of a melt-mediated process also provides several advantages over homogenous furnace annealing as well as CW, solid phase techniques. These include increased efficiency for large scale fabrication due to single shot batch processing capabilities (i.e. no rastering), increased control over the resulting microstructure, and features with sharp boundaries between irradiated and adjacent unirradiated film areas. The pulsed process is also advantageous as it may be performed on device films *in situ* in fairly close proximity to other possibly thermally sensitive components.

2.1 Transformation Thermodynamics

In order to successfully grade the shape memory response, a deep understanding of the physical parameters that govern the response itself is necessary. The transformation may be described thermodynamically via a Gibbs free energy formulation. Thus the near equilibrium trans-

formation proceeds upon a decrease in total free energy, i.e. $\Delta G^{A \to M} < 0$, and therefore $G^M_{tot} < G^A_{tot}$. The change in free energy is described as:

$$\Delta G^{A \to M} = A\gamma + V\Delta G_{strain} - V\Delta G_V \qquad (1)$$

where A, γ, V, ΔG_{strain} and ΔG_V are the interfacial area, interfacial free energy per unit area, volume, change in strain energy per unit volume and change in volumetric free energy per unit volume respectively. Therefore, for no externally applied stress, there exists an equilibrium temperature, T_{eq}, at which the volumetric free energies of the respective phases are equal. However, due to the formation of new interfaces as well as strain energy due to transformation, additional driving force is necessary for the transformation to proceed, and thus the transformation actually requires some degree of supercooling. The Gibbs free energy of the individual phases may be described as:

$$G = U + PV - TS - \sigma : \varepsilon \qquad (2)$$

where U, P, V, T, S, ε and σ are the internal energy, pressure, volume, temperature, entropy, and strain and stress (uniaxial) respectively. Also, at equilibrium (at a constant pressure) the free energies of martensite and austenite are equal such that $G^M = G^A$ and $dG^M = dG^A$. Combining with eq (2), one obtains a Clausius-Clapeyron type equation:

$$\frac{d\sigma}{dT} = -\frac{\Delta S}{\varepsilon^t} = -\frac{\Delta H}{T_{eq}\varepsilon^t} \qquad (3)$$

where ε^t is the strain associated with the transformation. This relationship is central to the mechanism proposed for functionally grading the phase transformation temperature. In essence it describes the rate with which the equilibrium phase transformation temperatures for a given alloy composition, change as a function of the stress state in the solid. Therefore, by locally controlling the stress state, one can effectively control the temperatures over which the phase transition will occur. Figures 1(a,b) depict this schematically.

2.2 Experimental Setup

NiTi films were deposited by simultaneous co-sputtering from an alloyed NiTi target and pure titanium target at powers of 302 and 50 watts respectively at an argon pressure of 3 mTorr resulting in films 200nm and 1μm in thickness. The films were deposited on a 1μm ultra-low residual stress silicon nitride (Si_3N_4) barrier layer that had been deposited on a [100] silicon wafer via low pressure chemical vapour deposition (LPCVD). The deposition was performed at room temperature, and thus resulted in an amorphous as deposited configuration. The 1μm films were subsequently annealed at 460° C for five minutes in a vacuum furnace, resulting in fully crystalline films. X-ray diffraction spectra were taken at room temperature and
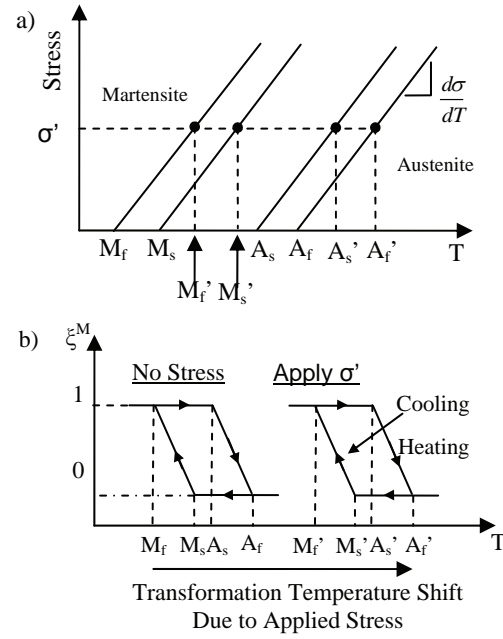

Figure 1: (a) Stress-temperature phase diagram. (b) Volume fraction of martensite as a function of temperature for the unstressed and stressed cases.

100° C confirm the film is martensitic at room temperature, and transforms to austenite at elevated temperatures. Furthermore, the film composition as Ti-51.8 at.% and Ni-52.4 at.% for the 1μm and 200nm films respectively was obtained via a calibrated electron microprobe.

Films were processed via pulsed irradiation using a 308 nm wavelength, XeCl excimer laser with 30 ns pulse duration over a wide range of incident laser energy densities. Energy density was uniform within the irradiated region whose geometry was a square, 320X320 μm. The laser system is synchronized with the underlying XYZ motion system such that a series of energy densities may be applied producing a spatial array on a single specimen. Each square region is an irradiated area of a single uniform energy density with 10 μm spacing. Additionally, a 632nm HeNe laser and photodiode were used *in-situ* in order to capture the time resolved transient reflectance of the irradiated region. 200nm thick samples were used to determine the effect of substrate temperature on the resulting crystallized films and were processed within a hot stage with a controlled atmosphere of argon at up to 800° C.

2.3 Thin Film Melting Regimes

The process of thin film melting may be generally described by three distinct energy density regimes as developed by Im *et. al* [7]. These regimes are defined by the extent to which the film has been melted through the thickness. At low energy densities (relative to thermal, thermodynamic as well as specimen configuration), the laser energy absorbed by the film is not sufficient to completely melt the film through the thickness and is termed the *partial melting* (PM) regime. In this case, for pre-crystallized films, resolidification proceeds via vertical re-growth from the remaining un-melted solid seeds. Microstructures in this regime are characterized by grain sizes remain on the order of the film thickness, and the substrate does not directly participate.

At high energy densities, the energy provided by the laser is sufficient for complete through-thickness melting. This is the *complete melting* (CM) regime. For flood irradiated areas, solidification proceeds along two paths. The first is lateral epitaxial growth at the boundary of the irradiated area where adjacent solid seeds grow into the significantly undercooled melt resulting in long, high aspect ratio crystals. The other path is via nucleation and subsequent growth. This occurs away from the boundary of irradiation and results in planar, equiaxed grains. Microstructures in this regime thus consist of laterally grown grains at the boundary, and nucleated grains whose diameters can greatly exceed the film thickness.

The final regime is the *near complete melting* (NCM) regime, and as the name suggests occurs over energy densities through which partial melting transitions to complete melting. Due to local inhomogeneities, for energy densities near the complete melt threshold (CMT), there are portions of the film that are completely melted and portions that are only partially melted. In this case solidification proceeds via two routes. The molten portions of the film go through nucleation and growth, while the near-complete melted seeds grow immediately upon reaching only slight undercoolings. The resulting grain size distribution is characterized by a bi-modal character with small grains having resulted from nucleation and growth, and large grains stemming from the remaining solid seeds that had additional time for growth before being arrested by surrounding nucleants.

2.4 Microstructure

Figures 2(a-f) are micrographs obtained via scanning electron microscopy (SEM) for specimens processed at 800° C. Figures 2(a, c, e) and 2(b, d, f) are obtained from laser treated areas away from and at the boundary of irradiation respectively. The microstructures presented in these figures have also been quantitatively analyzed, and both grain size and representative grain size distributions as a function of %CMT are found in Fig. 3. Although the micrographs presented here are limited to the 800° C substrate case, the 600° C and 700° C microstructures have been analyzed, and follow the same phenomenological trend (i.e. PM, NCM and CM transitions). Figures 2(a, b) are micrographs representative of the resulting microstructures processed at energy densities within the PM regime. This is seen by the reduced grain size, i.e. grain sizes restricted by film thickness, as well as the fact that no lateral growth is present at the irradiated boundary. The detail provided in Fig. 3 at 78% CMT reveals an average grain size and distribution. Figures 2(c, d) are micrographs obtained from specimen laser treated at 99% of the CMT. A significant increase in average grain size, as well as a transition to a bi-modal grain size distribution is in both the micrographs and detail in Fig. 3. In addition, the presence of some lateral growth is seen at the boundary as may be expected in the NCM regime. Finally, Figs. 2(e, f) are micrographs from specimen laser treated at 102% of CMT. Average grain size diminishes substantially, and the character of the grain size distribution changes to a single mode, log- normal distribution (see detail in Fig. 3). Most importantly however, is the presence of well defined lateral growth at the boundary which is direct evidence of film having
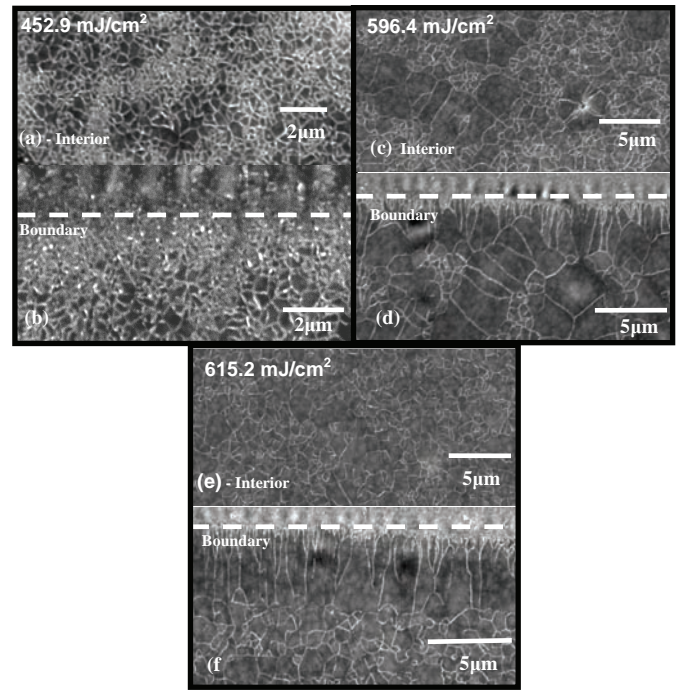

Figure 2: Scanning Electron Micrographs, $T_{substrate}$=800° C: Interior and boundary regions respectively. (a,b) Partially melted film characterized by small grain size limited to film thickness, ED=452.91 mJ/cm^2. (c,d) Near complete melting regime characterized by bi-modal grain size distribution, ED=596.4 mJ/cm^2. (e,f) Completely melted film characterized by the presence of large aspect ratio, well defined lateral growth, ED=615.2 mJ/cm^2.

undergone complete melting, and therefore nucleation and growth [7,8].

2.5 Transient Reflectance and Melt Depth

An understanding of the melting and resolidification process, specifically the relationship between the laser energy density is central in successfully predicting and spatially controlling phase transformation temperatures. This study is restricted to ultimate melt depths less than that of the film thickness. Figure 4a-d are several representative transient reflectance spectra obtained *in-situ*
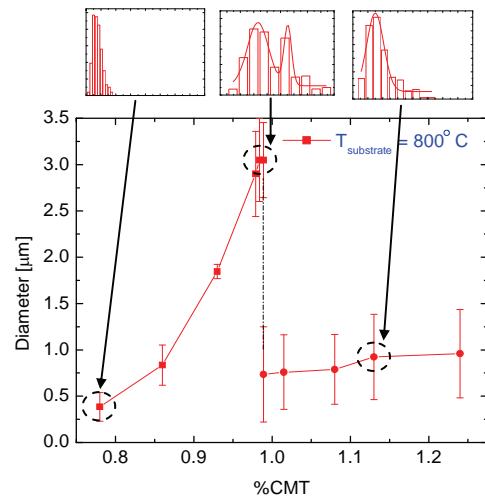

Figure 3: Average grain size as a function of % Complete Melt Threshold (CMT). Note the evolution of grain size distribution as the energy density transitions through the partial, near complete and complete melting regimes.
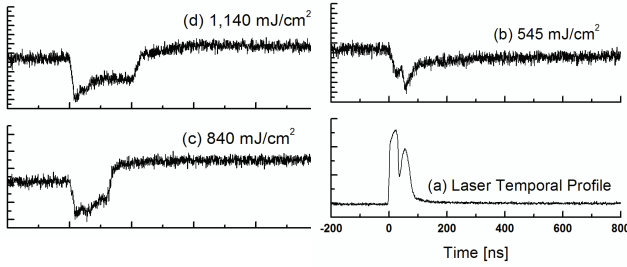
Figure 4(a-e): Transient reflectance spectra using a 632nm HeNe probe and photodiode obtained *in-situ* during laser irradiation for (b) 545 mJ/cm^2, (c) 840 mJ/cm^2, (d) 1,141 mJ/cm^2 and (e) 1,140 mJ/cm^2. The actual laser temporal profile (a) was obtained via a different photodiode.

Fig. 6(a-d): As-annealed NiTi film (representative): **(a)** Fully martensitic at room temperature, **(b)** upon heating, the martensite to austenite transformation begins for an A$_s$=45.1° C, **(c)** the transformation is complete, A$_f$=59.0° C and **(d)** upon cooling, the martensite to austenite begins, M$_s$=41.6° C.

during laser irradiation. Figure 4a is the actual temporal profile of the laser as captured by an additional photodiode. It is important to note that since the extinction depth (1/e^2) for NiTi is approximately 56nm, the signal may be seen as a reflection exclusively from the film surface with essentially no volumetric interaction. For Figs. 4(b-d), the initial reflectance (t<0) represents that of the solid, crystalline film. Upon irradiation a steep drop in reflected signal occurs representing surface melting. A subsequent plateau is observed, followed by a steep increase back to near the initial reflectivity value. The length of the plateau represents the time that the film surface remained molten.

Figure 5 is a plot of melt duration as a function of energy density. A discontinuity in slope is observed at approximately 1,350 mJ/cm^2. This discontinuity stems from the film having undergone complete, through thickness melting. Therefore, in order to solidify, nucleation must occur prior to grain growth. An average interface velocity of 6.5 m/s may now be determined from this by assuming a sharp interface, and traveled a total of 2μm (melt and regrowth) in approximately 300ns. If a constant average interface velocity is assumed for each irradiation, the energy density dependence of the melt depth may then be calculated. This is also plotted in Fig. 5.

2.6 Partial Melting Process

It is well documented [9,10] that solid phase crystallization of sputter deposited NiTi films via furnace annealing results in significant tensile residual film stress upon cooling to room temperature. The residual stress is composed of components from intrinsic stress due to lattice mismatch at the film/barrier layer interface, thermal expansion coefficient mismatch and volumetric contraction due to
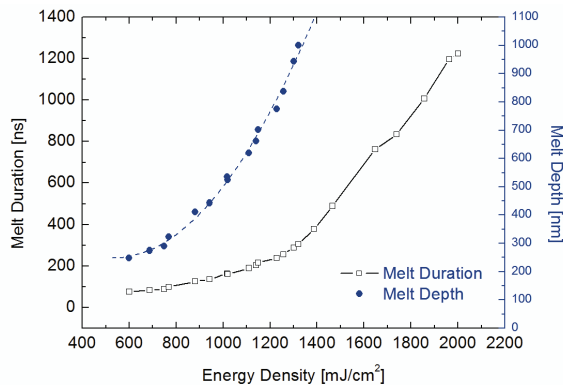
differences in molar volume between the amorphous and crystalline phases [11]. It has been reported however [12, 13] that the major contributor is the thermal stress developed upon cooling down, as the coefficient of thermal expansion of NiTi is as much as four times that of silicon and silicon nitride. Therefore, for a film of fixed composition, the resulting phase transformation temperatures will be shifted according to the residual stress state that develops in the film. Upon irradiation, the residual stresses in the molten region are completely relaxed. Vertical epitaxial regrowth from remaining crystals occurs upon reaching the equilibrium melting temperature until the entire molten region is again solid. The re-solidified layer begins to cool, and upon doing so, develops a new stress field due to thermal contraction. The stresses that develop are proportional to the change in temperature between the equilibrium melting temperature and room temperature, and are inversely proportional to the cross sectional area of the region, and therefore the ultimate depth of melting. A mechanism by which the phase transformation temperatures may be locally controlled via laser irradiation is proposed for the melted region, since $d_{melt} \sim E_{laser}$, $\sigma^m \sim 1/d_{melt}$ and $M_s \sim \sigma$:

$$M_s \sim \frac{1}{E_{laser}} \qquad (6)$$

Figure 5: Plot of melt duration as a function of energy density as obtained via transient reflectance analysis. Also plotted is the melt depth vs. energy density.
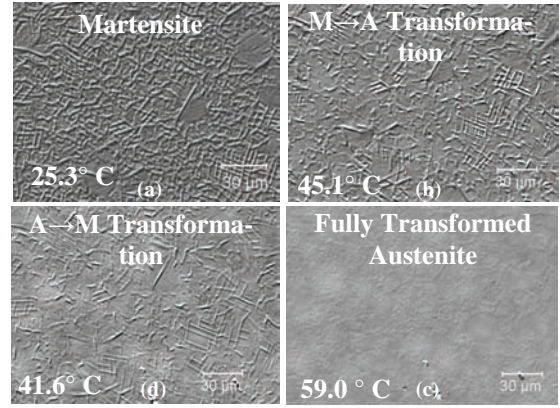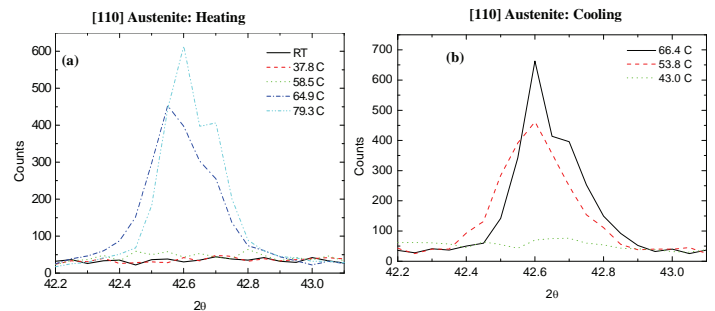

Figure 7(a, b): Typical X-ray diffraction spectra collected from unprocessed, as-annealed film revealing the emergence and disappearance of the [110] austenite peak upon (a) heating and (b) cooling.
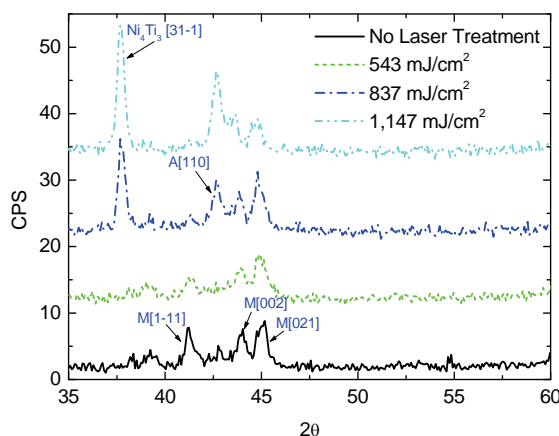
Figure 8: XRD spectra taken at room temperature revealing the phase(s) present as a function of laser energy density. Note the disappearance of the martensite [1-11] peak accompanied by the emergence of the austenite [110] and Ni_4Ti_3 [31-1] peaks.

Figure 9: Martensitic phase transformation temperatures as a function of incident laser energy density. Note the monotonic decrease for all start and finish temperatures. Also note the fact that the martensitic finish temperatures for the 837 and 1,147 mJ/cm^2 cases (not shown) drop below room temperature, explaining the residual austenite observed in Fig. 9.

The irradiated area of the film is confined to the desired geometry of the projection mask, and thus in-plane grading has been accomplished as well.

2.7 Surface vs. Volume

Phase transformation temperatures were characterized via *in-situ* temperature controlled optical microscopy which provides information regarding the transformation characteristics of the film surface and x-ray diffraction (XRD) which provides volumetric data. This is a particularly effective characterization scheme as two distinctive zones result from laser processing; the upper melted and resolidified region, and the underlying un-melted portion of the film. Characterization of the as annealed film (no laser processing) was performed in order to establish a baseline set of phase transformation parameters. Figures 6 (a-d) and 7(a,b) are optical micrographs and XRD spectra upon heating and cooling. Note that the optical micrographs reveal (via visual inspection) the surface transformation (martensite to austenite) initiating at approximately $A_s = 45.1°$ C. Full transformation is observed by $A_f = 59.0°$ C, and the reverse transformation starts at $M_s = 41.6°$ C and $M_f = 32.3°$ C. Figures 7(a,b) are XRD spectra taken across the 2θ range of the [110] austenite peak. They reveal $A_s \approx 65°$ C, $A_f \approx 79°$ C, $M_s \approx 54°$ C and $M_f \approx 43°$ C. The phase transformation temperatures differ as much as $20°$ C as observed by microscopy and XRD.

Wu et. al [11] report a substantial through thickness stress gradient in sputter deposited, furnace annealed NiTi films stemming from lattice mismatch. The maximum stress is located at the interface and decreases monotonically as the traction free film surface is approached. This stress gradient results in a corresponding gradient in phase transformation temperature, explaining the reduced phase transformation temperatures at the surface observed via microscopy, relative to those obtained through XRD.

2.8 Energy Density Effects

Figures 8 shows room temperature XRD spectra collected from films that have been laser processed at successively increasing laser energy densities. Note the
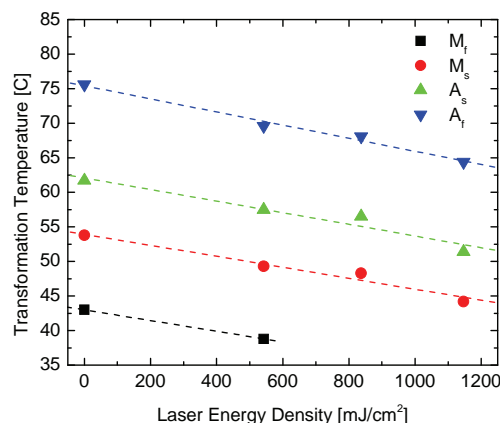
unprocessed films consist primarily of varying oriented martensite. However, upon laser processing over increasing energy densities, the [1-11] martensitic peak vanishes, while the [110] austenitic and [31-1] Ni_4Ti_3 peaks progressively emerge. Since there was no Ni_4Ti_3 detected in the unprocessed specimen, the formation of the metastable phase is a result of the highly non-equilibrium resolidification and is assumed to only be present in the melted and resolidified layer. In fact, a previous study performed by Birnbaum et. al. [14] on completely melted amorphous NiTi films revealed the appearance of nucleated and grown highly textured [31-1] Ni_4Ti_3. The emergence of the [110] austenite peak, however, is believed to be due to the local stress relaxation caused by the melt and solidification process. Its appearance suggests a decrease in phase transformation temperatures, thus acting to stabilize the austenite at the expense of the [1-11] martensite. This further supports the mechanism proposed in the preceding section as the peak intensity of the austenite peak also grows, accounting for a greater volume fraction, as energy density is increased.

Figure 9 shows the phase transformation temperatures as obtained from XRD spectra processed with varying energy density. The emergence and disappearance of the [110] austenitic peak was used to gauge the start and finish temperatures. It is seen that this occurs at successively lower temperatures until the [110] peak may be seen at room temperature (without any heating). This room temperature emergence is seen upon an incident laser energy density of 837 mJ/cm^2. Essentially what has happened is that the phase transformation temperature is dropping below room temperature, thus stabilizing the austenite and destabilizing the martensite. This observed decrease in phase transformation temperature is indeed consistent with the mechanism proposed in the previous section. This increased depth of melting and subsequent incremental drop in stress and concomitantly in martensitic phase transformation temperature.

3. Laser Surface Modification of Polymer

Biodegradable polymers have generated considerable interest due to wide-ranging applications. Poly (α-hydroxy acid) family of polymers, especially poly (lactic acid) (PLA), and its copolymers with poly (glycolic acid) (PGA) are particularly attractive since they are approved by the USFDA (United States Food and Drug Administration) and demonstrate high strength and high modulus. They degrade, primarily hydrolytically, in physiological and other environments to produce bioabsorbable products. These have been used extensively in drug delivery devices, fixation plates and pins, and tissue engineering scaffolds with promising uses in packaging and agriculture. While publications on biodegradable polymers are numerous, good reviews on PLA can be found by Garlotta [15] and Auras, et al. [16] discussing the structure, properties and crystallization behaviour of PLA.

Since the degradation (over 6 months to 3 years) and mechanical properties of PLA are strongly influenced by the sample crystallinity, there is a need for surface modification techniques to create interfaces with suitable properties to meet specific biomedical applications. Tsuji and Ikada [17] have studied the hydrolysis of PLA with varying crystallinity and concluded that PLA chain hydrolysis initiates in the amorphous regions within and between the spherulites.

Properties of PLA can be altered with either bulk or surface modifications. Bulk processes have the potential to affect only overall properties; so while overall degradation rate may be affected, degradation profiles are difficult to control. While surface treatments methods like coating, chemical modifications and plasma treatment have been shown to affect cell affinity, no surface structural modifications have been attempted as these methods are inherently difficult to control spatially [18]. More recently, laser processing of biodegradable polymers has generated interest. However, the main focus of several authors has been micro and nano-scale fabrication or study of surface properties like wettability [19, 20]. Laser treatment as a means of surface modification is attractive due to its flexibility, ease of use and spatial control.

The primary subject of this work is to utilize laser irradiation to reduce the crystallinity at the surface of PLA films, which can allow for more control over the degradation profile especially with increased contribution towards initial surface erosion from amorphous regions. Microscopy, Wide Angle X-ray diffraction (WAXD) and Fourier Transform Infrared (FTIR) Spectroscopy are used to study the morphology, crystallinity and short and long-range conformation changes.

3.1 Polymer Structure

High Molecular weight PLA is a colorless, stiff, thermoplastic polymer with a glass transition of ~ 60 ˚C and melting temperature of the order of 170-210 ˚C; which is higher than most low-melting polymers, making it suitable for thermal processing. PLA can exist as isomers poly-L-lactide (PLLA), poly-D-lactide (PDLA) or poly-DL-lactide (PDLLA); of which PLLA is semicrystalline due to its tacticity while PDLA is amorphous. PLLA can be crystallized by slow cooling from melt, annealing at various tempera-

tures above glass transition and under strain. Semicrystalline polymers such as PLLA are known to crystallize by chain folding forming lamellae perpendicular to the chain axis and thickness of the order of 10-30 nm.

To consider the effect of laser processing on PLLA, it is important to understand the structure, melting and crystallization of polymers in general and PLLA in particular. During nanosecond laser irradiation, short laser pulses can cause rapid heating and melting with cooling rates significantly higher (10^8 – 10^9 K/s) than traditional thermal processes. The total amount of the structural change in the material is a function of inception of nucleation and propagation (growth) which are a strong function of the undercooling and hence cooling rate. Non-isothermal crystallization studies of PLLA have shown that the kinetics of melt crystallization of PLLA are relatively slow as compared with other semi-crystalline polymers and hence the potential to affect its crystallinity using laser processing [21].

3.2 Polymer Crystallization

While thermodynamics of melting are relatively well understood, its kinetics are still under deliberation. In polymers, the melting transition occurs over a temperature range, with the equilibrium melting temperature defined in terms of the energy of the free surface using the *Gibbs-Thompson Equation* and varies with the thickness distribution of the lamellae in the material. Laser heating is rapid in comparison with traditional processes and while reversible melting is expected for quasi-isothermal processes, non-isothermal conditions with superheating such as laser irradiation allow for irreversible melting. With rapid melting, chains undergo a sudden increase in entropy and radius of gyration while and the melting rate is an increasing function of temperature. In general, melting is a fast process that is completed with low superheating as compared with crystallization which is a relatively slower process that needs a high supercooling [22, 23].

Nucleation is a controlled by undercooling and follows a bell shaped curve that reaches a maximum at the crystallization temperature which is of the order of 105-110˚C in PLLA. During laser processing large deviations from the melting temperature occur and hence the final development of crystallinity is expected not to be limited by the nucleation barrier but growth kinetics. In case of PLLA, primarily regime II growth (high nucleation rate with low growth velocity) is seen during isothermal crystallization with peak growth rates of the order of 2-5 μm/ min [21].

3.3 Experimental Setup

PLLA powder samples with less that 0.01% residual solvent and less that 0.01% residual monomer were obtained from PURAC© America. Films of nominal thickness of 20um (+/- 10um) were prepared by solvent casting and similar thickness specimens were selected for each experiment. PLA granules were dissolved in methylene chloride (0.1g/3ml, Sigma Aldrich©), stirred constantly for 3 hours using a magnetic stirrer, cast in a glass dish and left to settle for 10 hours at –20 ˚C. The film was cut into 15mm x 15mm squares, dried for 24 hrs prior to use [24] and subsequently annealed at temperatures of 110 ˚C and 135 ˚C for 3 hours. Amorphous samples were prepared by melting

films at 200 °C (3 min) between cover slips and subsequent quenching by placing in dry ice.

The experimental set-up consists of a 0.5 W Q-switched Nd: YAG laser operating at 355 nm in TEM00 mode utilized as the light source with a 50 ns pulse duration and1 kHz repetition rate. The laser scan velocity is governed by synchronized motion stages and optimized at 0.3 cm/s. 28 µm diameter beam was used with fluence varying from 30-50 J/cm^2. The sample was placed in a holder on computer-controlled XY stages and a 0.9 cm x 0.5 cm area treated in open air. Ultraviolet (UV) laser at 355 nm was selected as irradiation at longer UV wavelengths allows for primarily thermal effects (as the photon energy is below the bond breaking energy of C-C and C-H bonds) as opposed to photochemical bond breakage at shorter wavelengths and allows for greater affected depth due to absorption coefficient dependence on wavelength [20].

3.4 Characterization

The morphology of PLLA films was observed in transmission mode using a high resolution optical microscope (Nikon Eclipse). The microstructure of the microtomed sample cross-section was also observed with the aid of a scanning electron microscope (JEOL JSM-5600 LV) at voltages of 3-5 kV after gold coating (4-6 min). For SEM observation thicker 300 µm thickness samples were used for ease of microtoming. WAXD measurements were carried out using an Inel X-ray diffractometer. Film specimens were exposed to monochromatic Cu Kα radiation (λ=1.542 Å) at 30 kV and 30 mA and the scattered intensity measured in the Bragg angle range (2θ) from 10 to 90°. Mass Absorption Coefficient calculated for PLLA indicates that X-rays penetrate through the bulk of the film.

Thermo-Nicolet FTIR spectrophotometer with ATR (attenuated total reflectance) attachment using a ZnSe crystal at a fixed angle of 45° was used for measuring the IR spectrum of the samples, the data recorded with a 4 cm^{-1} resolution (averaging over 128 scans) and analysed by Omnic software. ATR technique of IR spectroscopy was utilized for measurement of sample spectra. ATR correction was applied to all spectra to normalize the effect of wavelength dependence. The morphology of the solution cast and annealed polylactide films observed under the optical microscope is shown in Fig. 10. The micrographs indicate crystalline films with formation of spherulitic crystallites with polygonal interfaces. The crystallite size is ~3 µm for 110°C annealed specimens. The film cross-section under
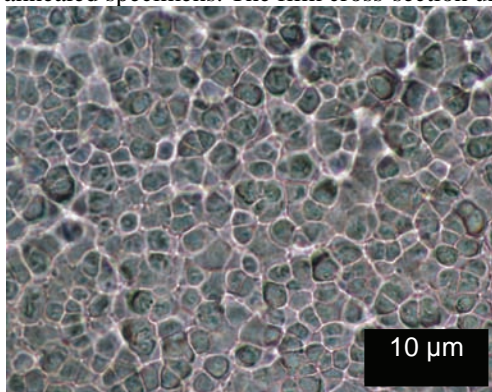

Figure 10: Optical transmission micrograph of sample PLLA film annealed at 110° C.

the microscope suggests that these are likely 3-D structures, stacked through the thickness. Similar morphology was observed under SEM.

3.5 Effects on Long-Range Order

The crystal structure of PLLA has been well studied and three different crystal modifications are seen; viz the α-form, β-form and γ-form depending on processing conditions. The α-form is the most commonly observed polymorph seen both for solution cast and melt processed samples with an orthorhombic unit cell with 2 10$_3$ (3 monomeric units per 10 Å rise) polymeric helices [25, 27]. The X-ray diffraction profile of PLLA annealed at 110 °C along with the treated sample (40J/cm^2), amorphous sample and background scatter are shown in Fig. 12. Crystallinity of the samples was determined based on simplifications of the *Ruland Method* as discussed by Alexander and Campbell [28, 29].

The background scattering was separated and amorphous fraction fit using a Gaussian profile as shown in Fig. 11. The fitted amorphous profile was scaled accordingly to fit the baseline of the measured diffraction patterns at different laser fluences. Mass fraction of the crystalline phase (X_c) was obtained by dividing the total intensities of the crystalline reflection with the total intensity between 2θ = 14° and 22°. The disorder factor due to lattice defects and thermal disorder was not considered in the calculations. The most prominent peak is seen at 16.7° which represents the (110) and (200) reflections and smaller peaks are seen at 14.7° and 19.1° representing planes with miller indices of (010) and (203) respectively. This agrees with the α-form of PLLA in line with other observations in literature for solution grown crystals.

Crystallite thickness can be measured using the *Scherrer equation* [30], $t_{hkl} = \dfrac{k\lambda}{B_{hkl}\cos\theta}$ where, t_{hkl} is the crystallite size perpendicular to the plane (*hkl*), *K* is the crystallite shape factor (0.9), λ is the wavelength, B_{hkl} is the width at half-maximum and θ the Bragg angle. For samples annealed at 110 °C, the crystallite thickness was measured to be in the range of 15-20 nm using the (110/200) reflection as seen in Fig. 12. Effects of laser fluence (30-50 J/cm^2) have been studied to allow for processing control by simply changing the laser power.
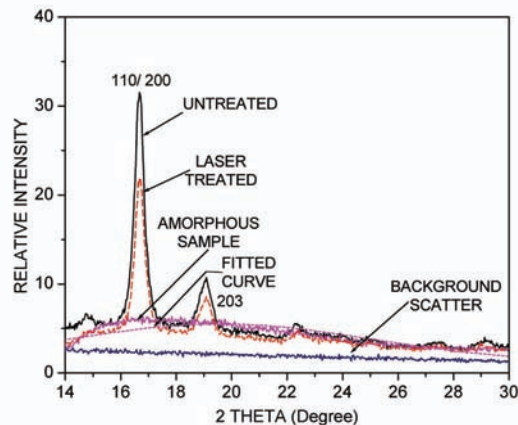

Figure 11: WAXD Profiles of Untreated sample annealed at 110 °C, Laser Treated (40 J/cm2), amorphous sample and background scatter. Note reduction in 110/200 and 203 peaks.
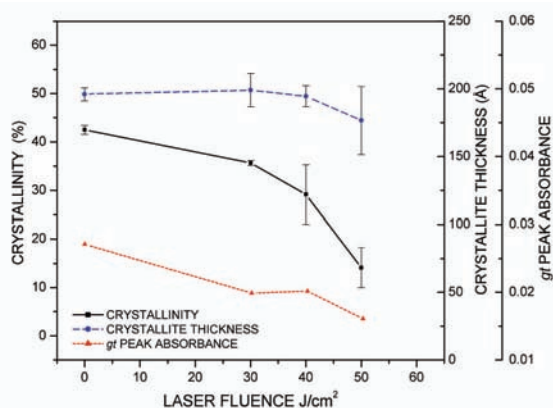
Figure 12: Effect of Laser Fluence on the Crystallinity and Crystallite thickness of PLLA film samples obtained from WAXD and *gt* peak absorbance values from curve fitting of Carbonyl region of FTIR spectra.

Figure 13: WAXD Profiles indicating effects of laser fluence on the long range order of PLLA sample. Profiles represent the crystalline fraction in the material. The variation of crystallinity with fluence can be seen in Fig. 13.

The WAXD profiles of the crystalline fraction of untreated sample and sample irradiated at various laser fluences are shown in Fig. 13. There is a reduction in the intensity of both (110/200) and (203) peaks. The (110/200) peaks show increasingly reduced intensity with increasing fluence which indicates that the laser treatment primarily resulted in reduced order perpendicular to the helical chain direction *c* and hence sample crystallinity.

Figure 12 indicates the effect of laser treatment at different fluences on the measured mean crystallinity and crystallite thickness of the sample (bar indicates standard error). The crystallinity of the sample was reduced by 7-8% for lower intensities to almost half the original value at higher fluences. Since, WAXD provides integral intensity data from the complete depth of the sample film (see Section III.C), this can be attributed both to increased energy input causing melting of crystallites at progressively increasing depths in the sample films and more complete melting at higher temperatures in the surface regions.

The crystallite thickness is not observed to change considerably. However, as seen in Fig.12, mean crystallite thickness reduces at higher fluences which indicates that disruption of structure might stem from partial melting at lower fluence regimes and more complete melting of high melting crystals at higher fluence, causing random displacements. This would explain why no significant broadening occurs in the XRD profiles and the main effect seen on irradiation is a reduction in the measured intensity.

Figure 14 shows the SEM images of the untreated 300 μm sample and those treated at 30 and 50 J/cm² respectively. While no direct melting regions can be distinguished, it is apparent that there the affected depth increases with increased fluence. Crazing in 3D in thick parts has been widely observed in semi-crystalline polymers and it has been suggested [30] that the crazes are initiated between the amorphous regions zones between the crystal lamellae which is in accordance with our observations.

3.6 Effects on Short Range order using Infrared Spectroscopy

FTIR spectroscopy provides considerable information regarding short range order in semicrystalline polymers including chain conformations, crystallinity and phase trans
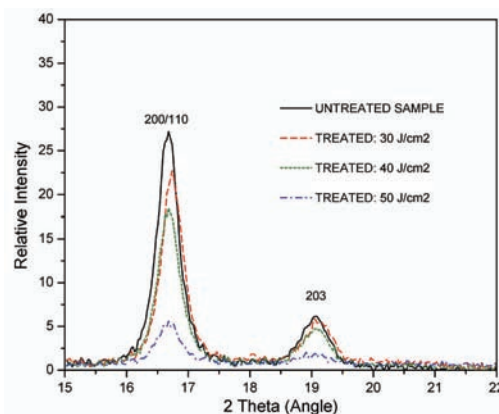
formations. In PLLA, the polymer back bone bond stretching and skeletal bending modes are sensitive to changes in chain conformation apart from changes owing to index of refraction and density transitions. New absorption bands appear due to lower molecular symmetry in a crystal field contributing to active vibrations or splitting of bands due to intramolecular interactions. ATR-FTIR spectrum of untreated, laser treated (30 J/cm²) and amorphous PLLA film are shown in Fig. 16. It can be seen that the Carbonyl (C=O) stretching region, CH_3 and CH bending region, and skeletal stretching (C-O-C) regions of original crystalline PLLA show sharper peaks with band splitting in carbonyl and C-O-C stretching regions and a band at 920 cm⁻¹ in accordance with observations in literature [31]. The PLLA monomer has three skeletal bonds C-O (ester), O-C_α and C_α-C; with the ester bond assumed to be *trans* due to electron delocalization. Minimum energy calculations by Brant, et al. [33] indicate four feasible rotational isomeric states: *t't, t'g,, g't* and *g'g* corresponding to *trans* angles of -160°, 160° (*t'* and *t*) and *gauche* angles of -73° and -48° (*g'* and *g*) respectively. Henceforth, only *g* and *t* have been used in the text and should be self-explanatory.
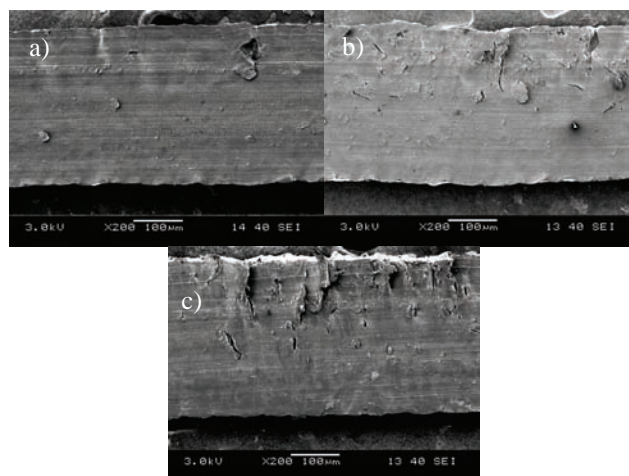

Figure 14: SEM images of 300 μm (a) untreated sample and samples treated at (b) 30 J/cm2 and (c) 50 J/cm2, indicating microtome induced crazing treated samples which is indicative of increase in the amorphous fraction in the polymer due to laser irradiation. Also, the affected depth increases with increase in fluence.
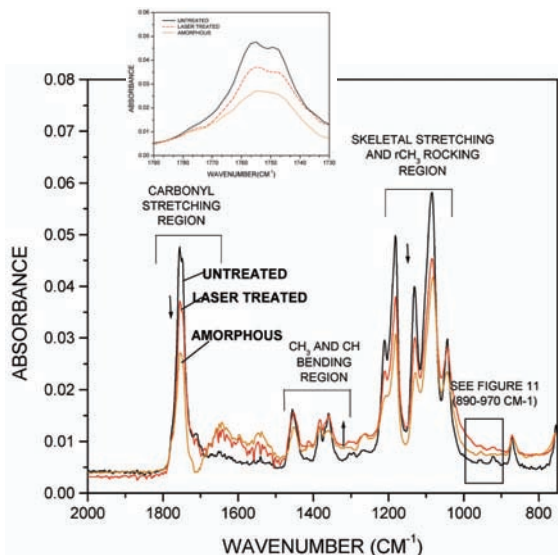
Figure 15: FTIR spectra of untreated specimen annealed at 110 ˚C, laser treated (30J/cm2) and amorphous specimens from 2000-700 cm-1 indicating the important bending, stretching and rocking modes of PLLA. Details of carbonyl stretching region (inset).

The *gt* conformers have the lowest energy and correspond to a 10_3 helix with the C=O groups perpendicular to the helix (E mode). While the simulated spectrum shows 55% *gt*, 37% *gg* conformers (straight conformers) and 4% each of other bent conformations [32]; experimentally *gg* conformers are seen to be much lower and with more *tt* conformers which give extended chains and do not challenge the stiffness shown in PLLA chains. Following this analysis, Meaurio, et al. [33] have observed that the carbonyl region of PLLA splits into four peaks during crystallization at 1776, 1767, 1759 and 1749 cm-1 corresponding to *gg*, *tg*, *gt* and *tt* conformations respectively primarily due to intra-molecular coupling.

The details of the C=O stretching region (1790-1730 cm-1) of the spectrum is shown inset in Fig. 15. Pronounced splitting is seen in the original sample with broad peak in the amorphous sample and the treated sample showing reduced splitting.

As can be noted negligible *gg* conformers are seen which correspond to a 4_1 helix; *gg* being the only conformation with C=O groups parallel to the helix (A mode). The CH_3 and CH bending region in Fig. 16 (1250-1400 cm-1) also indicates broader peaks due to laser irradiation.
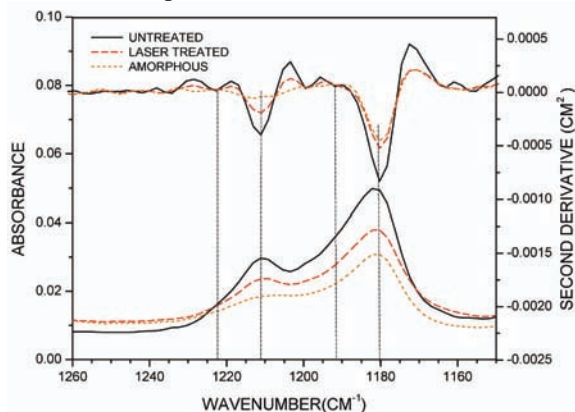

Figure 16: FTIR absorbance and derivative spectrum of the skeletal (C-O-C) stretching regions of PLLA. Lower crystalline perfection is seen in the samples represented by broader bands. The mean factor group splitting is seen at 1192 and 1222 cm-1.
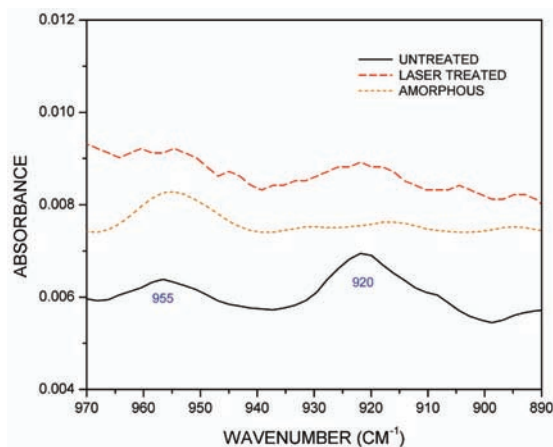

Figure 17: 970-890 cm-1 Region of FTIR spectrum indicating reduction in the band at 920 cm-1 (corresponding to coupling of the νC-C backbone stretch with CH3 rocking mode in 103 helical conformation of PLLA) with laser treatment.

The skeletal stretching region of PLLA (1050-1260 cm-1) and its derivative spectrum are shown in Fig. 16, consisting of asymmetric C-O-C stretching vibrations 1180 and 1210 cm-1 respectively parallel and perpendicular to the helix for the amorphous specimen. These modes split into 1180/1192 (A modes) and 1212/1222 cm-1 (E_1 modes) for the cold crystallized samples while reduced factor group splitting is seen in the laser processed samples suggesting reduced crystal perfection. As shown in Fig. 17 (970-850 cm-1 region) the band at 920 cm-1 reduces while peak at 955 cm-1 increases slightly upon laser processing with significant increase seen at higher fluences. The 920 cm-1 band was assigned [30] to coupling of the νC-C backbone stretch with CH_3 rocking mode in 10_3 helical conformation of PLLA.

As observed earlier, XRD indicates a 10_3 helical structure based on α-form of PLLA and from IR spectra the *gt* conformers represent the crystalline conformers. Hence, peaks corresponding to *gt* conformation can be used to understand the effect of laser processing. Using similar approach, the effect of laser fluence is demonstrated by comparing the reduction in peak heights of *gt* conformers as a function of the fluence as seen in Fig. 12 which follows the same trend as seen in WAXD. While this band is due to added contributions from the *gt* conformers in the crystal lamellae and the interphase regions, the reduction has to be attributed to conformation changes happening in the crystal domains of the polymer. The reduction is less drastic as compared with the WAXD peaks due to smaller d_p associated with IR spectrum in the carbonyl region. However, the reduction in conjunction with reduced lamellar thickness may imply transition from partial to complete melting at higher fluences in the layer at the surface probed by the ATR crystal.

4. Conclusions

It has been demonstrated that pulsed, melt mediated laser irradiation is in fact capable of modifying aspects of the thermodynamic, mechanical and shape memory responses of NiTi thin films. Furthermore, within the partial melting regime, martensitic phase transformation temperature decreases with increasing laser energy density. A melt-depth

controlled film stress mechanism is proposed to explain this phenomenon. As this process has been shown to successfully alter aspects of the film's shape memory response, it may now be applied in fabricating monolithic, functionally graded micro-scale devices.

It has also been shown that UV nanosecond laser irradiation at 355nm can be used to reduce the crystallinity of aliphatic homopolymer L-PLA, by primarily affecting a layer at the surface of the sample. Laser processing affects both long and short range order in the polymer. Rapid melting at the surface, quench rates in the process, which are determined to be of the order of 10^6 K/sec; multiple thermal cycles, superheating and heat accumulation due to pulsed nature of the process and primarily regime II kinetics of PLLA contribute to an overall reduction in crystallinity in the material and partial melting may be an important contributory factor. Final crystallinity has also been shown to be a function of the laser fluence. Hence, laser surface treatment would allow for a controllable, practically applicable and automated process that can spatially control the surface morphology and hence degradation and other properties associated with a different crystallinity at the surface.

These two applications of laser surface modification are a strong example of the versatility of laser processing in changing the properties of various types of materials. While both processes focus on changing the structure of the films, one seeks to change the crystal structure of a metal to modify mechanical properties and shape memory characteristics while the other seeks to reduce the crystallinity of a polymer to exert fine control over degradation rates.

References
[1]   D.Y. Li: *Wear,* (1998) 221 p.116–123.
[2]   S. Gialanella, G. Ischia, and G. Straffelini: *Journal of Material Science,* (2008) 43, 1701–1710.
[3]   L. Tan, W.C. Crone, and K. Sridharan: *Journal of Material Science:Materials in Medecine, (2002)* 13, 501-508.
[4]   X. Wang, Y. Bellouard, and J.J. Vlassak: *Acta Materialia*, (2005) 53, 4955–4961.
[5]   Y. Bellouard, T. Lehnert, J.-E. Bidaux, T. Sidler, R. Clavel, and R. Gotthardt: *Materials Science and Engineering A*, (1999) 795–798.
[6]   Q. He, M.H. Hong, W.M. Huang, T.C. Chong, Y.Q. Fu, and H.J. Du: Journal of Micromechanics and Microengineering, (2004) 14, 950–956.
[7]   J.S. Im, H.J. Kim, and M.O. Thompson: *Applied Physics Letters*, (1993) 63, 1969-1971.
[8]   J.S. Im, and H.J. Kim: *Applied Physics Letters*, (1994) 64, pp. 2303-2305.
[9]   Y. Fu, and H. Du: *Surface and Coatings Technology*, (2002) 153, pp. 100–105.
[10]   Y.Q. Fu, S. Zhang, M.J. Wu, W.M. Huang, H.J. Du, J.K. Luo, A.J. Flewitt, and W.I. Milne: *Thin Solid Films*, (2006) 515, pp. 80 – 86.
[11]   T. Wu, B. Jiang, X. Qi, Y. Liu, D. Xu, and L. Wang: *Materials Transactions, Japan Inst. of Metals,* (2002) 42, pp. 566-570.
[12]   D.S. Grummon, J. Zhang, and T.J. Pence: *Materials Science and Engineering A,* (1999) pp. 722-726.
[13]   J.J. Gill, K. Ho, and G.P. Carmen: *Journal of Micro-electro-mechanical Systems,* (2002) 11.
[14]   A.J. Birnbaum, U.J. Chung, X. Huang, A.G. Ramirex, S. Polvino, and Y.L. Yao: *Proceedings of ICALEO- Laser Materials Processing,* (2007) *pp. 98-107.*
[15]   D. Garlotta: Journal of Polymers and the Environment, (2001) 9(2), pp. 63-84.
[16]   R. Auras, Harte, B and Selke, S.: Macromolecular Bioscience, (2004) 4(9), pp. 835-864.
[17]   H. Tsuji, and Y. Ikada: Journal of Polymer Sci., Part A: Polymer Chemistry, (1998) 36 (1), pp. 59-66.
[18]   W. Wang, W. Cui, and J. Bei: Analytical and Bioanalytical Chemistry, (2005) 381(3), pp. 547-556.
[19]   K.S. Tiaw, S.W. Goh, M. Hong, Z. Wang, B. Lan, and S.H. Teoh: Biomaterials, (2005) 26(7), pp. 763-769 .
[20]   S. Chen: Int. J. of Material & Product Technology, (2003) 18(4/5/6), pp.457-468.
[21]   R. Vasanthakumari, and A.J. Pennings: Polymer, (1983) 24(2), pp. 175-178.
[22]   B. Wunderlich: Macromolecular Physics, Vol. 2 (1976), Crystal Nucleation, Growth, Annealing and Vol 3. (1980), Crystal Melting, Academic Press, New York.
[23]   G.L. Liag, D.W. Noid, B.G. Sumpter, and B. Wunderlich: Acta. Polymer, (1993) 44, pp. 219-224.
[24]   C. T. Laurencin, et al.: Journal of Orthopaedic Research, (2002) 20, pp. 20-28.
[25]   J. Kobayashi, et al: J. Appl. Phys. (1995) 77(7), pp. 2957-2973.
[26]   C. Marega, A. Marigo, V. Di Noto, and R. Zannetti: Makromol. Chem., (1992) 193 (7), pp. 1599-1606.
[27]   L. Alexander: X-Ray Diffraction Methods in Polymer Science, (1969) Wiley-Interscience, New York.
[28]   D. Campbell, R.A. Pethrick, and J.R. White: Polymer Characterization, 2nd Ed., (2000) Stanley Thornes, Cheltenham.
[29]   K. Friedrich: Advances in Polymer Science, Crazing in polymers, (1983) 52/53, Kausch, H.H. (Ed.), Springer-Verlag, Berlin-Heidelberg
[30]   G. Kister, G. Cassanas, and M. Vert: Polymer, (1998) 39 (2), pp. 267-273.
[31]   D.A. Brant, A.E. Tonelli, and P.J. Flory: Macromolecules, (1969) 2 (3), 228-235.
[32]   S. Kang, S.L. Hsu, H.D. Stidham, P.B. Smith, M.A. Leugers, and X. Yang: Macromolecules, (2001) 34 (13), pp. 4542–4548.
[33]   E. Meaurio, E. Zuza, N. Lopez-Rodrıguez, and J.R. Sarasua: J. Phys. Chem. B, (2006) 110 (11), pp. 5790-5800.